

# Characterization of internal tide non-stationarity : Eulerian versus Lagrangian perspectives

Zoé Caspar-Cohen<sup>1</sup>, Aurélien Ponte<sup>1</sup>, Noé Lahaye<sup>2</sup>, Xavier Carton<sup>3</sup>, Xiaolong Yu<sup>1</sup>, and Sylvie Le Gentil<sup>1</sup>

<sup>1</sup>Ifremer

<sup>2</sup>Inria & IRMAR, campus universitaire de Beaulieu

<sup>3</sup>Université Bretagne Occidentale

November 21, 2022

## Abstract

The Lagrangian and Eulerian near-surface current signatures of a low-mode internal tide propagating through a turbulent jet are compared in an idealized numerical simulation. We estimate and compare internal tides' stationary and nonstationary velocity amplitudes as well as non-stationarity timescales. We find Lagrangian internal tides total amplitude similar to Eulerian one. Lagrangian velocity are mostly nonstationary and Lagrangian non-stationary timescales are comparable to or smaller than Eulerian ones. This low-bias is proposed to be the result of the deformation of internal tide surface signal along the drift induced by lower frequency surface currents. A model based on the latter hypothesis successfully predicts Lagrangian autocovariance and highlights its dependence to Eulerian autocovariance and to the properties of the internal tides and jet. We address the implications of these results in the context of the Surface Water and Ocean Topography (SWOT) mission, for which the separation of mesoscale balanced flow and internal tides with data at the ocean's surface was raised.

1 **Characterization of internal tide non-stationarity : Eulerian versus**  
2 **Lagrangian perspectives**

3 Zoé Caspar-Cohen\*, Aurélien Ponte

4 *Ifremer, Université de Brest, CNRS,IRD, Laboratoire d'Océanographie Physique et*  
5 *Spatiale (LOPS), IUEM,Brest,France*

6 Noé Lahaye

7 *Inria, IRMAR, campus universitaire de Beaulieu, Rennes, France*

8 Xavier Carton, Xiaolong Yu and Sylvie Le Gentil

9 *Ifremer, Université de Brest, CNRS,IRD, Laboratoire d'Océanographie Physique et*  
10 *Spatiale (LOPS), IUEM,Brest,France*

11 \*Corresponding author: Zoé Caspar-Cohen, zoe.caspar@ifremer.fr

## ABSTRACT

12 The Lagrangian and Eulerian near-surface current signatures of a low-mode internal tide  
13 propagating through a turbulent jet are compared in an idealized numerical simulation.  
14 We estimate and compare internal tides' stationary and nonstationary velocity amplitudes  
15 as well as non-stationarity timescales. We find Lagrangian internal tides total amplitude  
16 similar to Eulerian one. Lagrangian velocity are mostly nonstationary and Lagrangian  
17 non-stationary timescales are comparable to or smaller than Eulerian ones. This low-  
18 bias is proposed to be the result of the deformation of internal tide surface signal along  
19 the drift induced by lower frequency surface currents. A model based on the latter  
20 hypothesis successfully predicts Lagrangian autocovariance and highlights its dependence  
21 to Eulerian autocovariance and to the properties of the internal tides and jet. We address  
22 the implications of these results in the context of the Surface Water and Ocean Topography  
23 (SWOT) mission, for which the separation of mesoscale balanced flow and internal tides  
24 with data at the ocean's surface was raised.

## 25 **1. Introduction**

26 The disentangling of internal tides and balanced flow is a key issue for the Surface  
27 Water and Ocean Topography (SWOT) mission (Morrow et al. 2019). This wide-swath  
28 altimeter mission will provide instantaneous 2D sea level maps, with an expected horizontal  
29 resolution of the order of 15–30 km (Morrow et al. 2019; Fu et al. 2012). With this  
30 resolution, internal tides and mesoscale balanced flow will be captured, providing a unique  
31 opportunity to study both motions and their interaction. While both motions have distinct  
32 time scales, they can have similar length scales (order of hundreds of kilometers) which  
33 makes their separation by spatial filtering difficult. SWOT coarse temporal resolution  
34 (20 day repeat time approximately) will also prevent a separation by temporal filtering.  
35 Due to these two issues, internal tides and balanced flow will be entangled in SWOT data,  
36 which is problematic for estimates of surface currents via geostrophy.

37 Internal tides (or baroclinic tides) are internal waves generated by the barotropic tide  
38 when it passes over a topography (Garrett and Kunze 2007). Internal tides that are phase-  
39 locked with the tidal forcing are referred to as stationary internal tides. Stationary internal  
40 tides are predictable as they are phase-locked and of known amplitude. A fraction of the  
41 internal tides energy (mainly high modes) dissipates close to their generation’s location  
42 (Whalen et al. 2020) but a significant part travels in the open ocean over potentially  
43 great distances – up to thousands of kilometers – with a low-mode vertical structure. As  
44 they travel, internal tides encounter variations of the background stratification as well as  
45 obstacles (continental shelf, islands, etc) which can cause energy dissipation or scattering  
46 toward higher modes (Whalen et al. 2020; Savva and Vanneste 2018; Savage et al. 2020).  
47 Internal tides can also become nonstationary. In particular, loss of stationarity has been  
48 observed when internal tides travel in a background stratification that varies in time  
49 (Buijsman et al. 2017), or pass through a turbulent jet (Ponte and Klein 2015; Dunphy

50 et al. 2017; Savage et al. 2020). They also become nonstationary when they reach the  
51 continental shelf (Nash et al. 2012b,a).

52 Several works used altimeter observations to study baroclinic tide including its non-  
53 stationary component (Ray and Zaron 2016; Zaron 2017, 2019; Nelson et al. 2019). To  
54 overcome limitations of altimeter data, the use of the global drifter program (GDP) dataset  
55 has been investigated in addition to the altimeter data (Zaron 2017, 2019; Nelson et al.  
56 2019). The GDP complete dataset, combining Argos and GPS localisation system, is  
57 available interpolated over a temporal grid of 1h (Elipot et al. 2016). Lately, the number  
58 of drifters localised via GPS has increased, with only GPS tracked drifters recently de-  
59 ployed, thus decreasing the localisation error in the data (Elipot et al. 2016). This dataset  
60 has already been used to investigate high frequency near-surface near-inertial oscillations  
61 (NIOs) (Elipot et al. 2010).

62 There are however challenges and questions raised by the use of Lagrangian data. One  
63 of the challenges associated with the analysis and interpretation of Lagrangian data is that  
64 data collected by a drifter as it moves along with the flow may entangle Eulerian spatial  
65 and temporal variability and, give a deformed perspective of the Eulerian field. (LaCasce  
66 2008) reviewed conceptual frameworks that have been developed in order to tackle this  
67 issue (Lumpkin et al. 2002; Middleton 1985; Davis 1983, 1985). Two regimes are typically  
68 identified : fixed float and frozen turbulence. The prevalence of one regime over the other  
69 is determined by the parameter  $\alpha = T_E/T_a$ , where  $T_E$  is the Eulerian evolution timescale  
70 of the flow and  $T_a$  is the time required for a drifter to travel the Eulerian characteristic  
71 spatial scale of the observed fluctuation.  $T_a$  is given by  $L/U$ , with U corresponding to an  
72 advection velocity and L the fluctuation's spatial scale. If  $\alpha \ll 1$ , the time required for  
73 the drifter to travel the length  $L$  is greater than the timescale of the fluctuation,  $T_E$ . In  
74 this case, one can expect an agreement between the Lagrangian and Eulerian timescales.  
75 Conversely, if  $\alpha \gg 1$ , it takes a drifter a time smaller than  $T_E$  to travel a distance  $L$ , causing

76 a more rapid fluctuation in the Lagrangian perspective. In this paper we apply these ideas  
77 to fit the case of internal tides interacting with a turbulent jet.

78 (Zaron and Elipot 2020) found a spectral broadening of the barotropic tide peaks in  
79 Lagrangian data compared to the Eulerian one, due to flow and/or tides spatial non-  
80 stationarity. It is therefore not trivial that Lagrangian drifter data may be used to study  
81 internal tides and their loss of stationarity depending on the regions of the ocean and the  
82 associated dynamical regime. It is also necessary to evaluate the use of Lagrangian data  
83 in the context of SWOT. Can Lagrangian data be used to filter and identify internal tides?  
84 In this study, we compare the non-stationarity timescales and amplitudes of an internal  
85 tide field crossing a turbulent jet, in Eulerian and Lagrangian frameworks. This allows us  
86 to test analytical models describing balanced flow and internal tides in an idealized set-up  
87 and the relationship of Eulerian and Lagrangian timescales.

88 We first present the numerical set-up used in this study as well as the method and model  
89 used to estimate signal amplitudes and decorrelation timescales. The results are shown in  
90 the second part for one simulation at first and several simulations varying the jet's strength  
91 later, . Lastly, we develop a theoretical model to predict Lagrangian autocovariance from  
92 Eulerian one and confront our results to it.

## 93 **2. Numerical simulations and Lagrangian data**

### 94 *a. Numerical simulations*

95 Idealized numerical simulations of an internal tide crossing a turbulent jet are considered.  
96 The numerical model is the Coastal and Regional Ocean Community model (CROCO)  
97 solving the hydrostatic equations. Its configuration follows Ponte et al. (2017) with a  
98 rectangular numerical domain (1024 km x 3072 km), zonally periodic. The Coriolis  
99 frequency follows the beta-plane approximation and is defined so that the domain is  
100 representative of mid-latitudes. A turbulent zonal jet crosses the domain at its center

101 along the meridional direction. It results from initialising the numerical simulation with a  
102 baroclinically unstable jet and is maintained by relaxing zonally averaged fields (velocities,  
103 temperature, sea level) toward the initial jet. Simulations with different turbulent jet  
104 strength are obtained by modulating the strength of the initial jet or equivalently the  
105 latitudinal thermal gradient. After 500 days, relaxation of the zonal mean fields toward  
106 the initial jet is ceased. The jet has a mean velocity amplitude maximum around 1450km  
107 in the center of the jet (Fig.1a, red line). The jet's amplitude decays over the observed  
108 period of time with a maximum around 0.6 m/s at the beginning and around 0.4 m/s at  
109 the end. The jet's velocity is computed by averaging each velocity component (u and v)  
110 over 2 days.

111 A mode-1 internal wave is generated at  $y = 400$  km with a semi-diurnal frequency  
112 (2 cpd). Its signature at the surface contributes significantly to the total velocity amplitude  
113 in the northern and southern areas (Fig.1a, green line compared to red line). Sponge layers  
114 are put on the top and the bottom of the domain ( $y < 300$  km and  $y > 2700$  km). About  
115 8000 simulated near surface drifters (referred to as drifters in the rest of this study) are  
116 also initialised at day 500 on a regular grid extending from 600 km to 2400 km and their  
117 advection is performed online (Fig.1b).

### 118 *b. Lagrangian outputs overview*

119 In the central part of the domain, the jet turbulence dominates the drifter net motion with  
120 a displacement of about 300 km in the  $x$ -direction and 160 km in the  $y$ -direction, i.e. an  
121 internal tide wavelength, over a 40 day time window (Fig.2c). When averaged over all  
122 drifters in this area, the net displacement over such time window is about 200 km. Away  
123 from the jet (Fig.2a and e), the net distance travelled by selected drifters, in the  $y$ -direction,  
124 is of about 20–30 km which is a fraction of an internal tide wavelength. Internal tides  
125 produce on the other hand periodical displacements of the order of 2–3 km. Eulerian

126 and Lagrangian zonal velocity time series exhibit significant differences in the jet at both  
 127 low and internal tide frequency (modulation of the envelope and phase) over the 40 day  
 128 temporal window (Fig2d). To quantify these differences, we will estimate amplitude  
 129 and decorrelation/nonstationary time scales associated with the jet and internal tides and  
 130 compare the results in different parts of the domain.

131 Zonal velocity time series outside the jet (Fig2b and f) exhibit weaker differences  
 132 between both perspectives, as seen from their envelopes. Modulations of internal tide  
 133 fluctuations in the south and north parts of the domain differ markedly from each other  
 134 with faster fluctuations of their envelope in the north compared to the south. This feature  
 135 occurs in both Eulerian and Lagrangian time series and reflects the loss of stationarity of  
 136 the internal tide as it propagates northward and interacts with the turbulent jet.

### 137 *c. Methods*

#### 138 1) ESTIMATION OF EULERIAN AND LAGRANGIAN AMPLITUDES AND TIMESCALES

139 We estimate the amplitudes and decorrelation timescales of slow and fast motions by  
 140 computing the velocity autocovariance in Eulerian and Lagrangian model outputs and  
 141 fitting it to a theoretical model for a superposition of two motions (fast and slow) keeping  
 142 timescales and amplitudes as variables. We assume a velocity component  $v$  may be written  
 143 as the sum of an internal tide part  $\tilde{v}$  and a turbulent (or jet) part  $\bar{v}$ :

$$v = \tilde{v} + \bar{v} \quad (1)$$

144 Assuming internal tide velocities and jet velocities are uncorrelated, the total autocovari-  
 145 ance,  $C$ , equals to the sum of the autocovariances of  $\tilde{v}$  and  $\bar{v}$  :

$$C(\tau) = \langle v(t)v(t+\tau) \rangle = \tilde{C}(\tau) + \bar{C}(\tau), \quad (2)$$

146 where  $\langle \cdot \rangle$  is a time averaging operator.

147 The high frequency signal for mode-1 internal tides is written as

$$\tilde{v} = \Re \left[ \tilde{v}_e(t) e^{i\omega t} \right] \text{ with } \Re \text{ the real part} \quad (3)$$

148 where  $\tilde{v}_e$  is the envelop of the oscillations of the tides and depends on the time, thus  
 149 capturing the non-stationarity of the waves.  $\omega/2\pi$  is the frequency of the waves, 2 cycles  
 150 per day.

151 The internal tide signal can be decomposed into stationary and nonstationary contribu-  
 152 tions. The stationary part is defined with a coherent temporal averaging operator :

$$\tilde{v}_s = \langle \tilde{v} \rangle_c, \quad (4)$$

$$= \Re \left[ \langle \tilde{v}_e \rangle_c e^{i\omega t} \right] \quad (5)$$

153 Hence the nonstationary part, defined as the total velocity minus the stationary part :

$$\tilde{v}_{ns} = \tilde{v} - \langle \tilde{v} \rangle_c, \quad (6)$$

$$= \Re \left[ (\tilde{v}_e - \langle \tilde{v}_e \rangle_c) e^{i\omega t} \right] \quad (7)$$

154 Assuming the envelope of the nonstationary signal is exponential with a decay timescale  
 155  $\tilde{T}$ , the fast autocovariance is expressed as:

$$\tilde{C}(\tau) = \left[ \tilde{V}_s^2 + \tilde{V}_{ns}^2 e^{-\tau/\tilde{T}} \right] \times \cos(\omega\tau) \quad (8)$$

156 Following Veneziani et al. (2004) the turbulent velocity autocovariance is assumed to  
 157 have the form :

$$\bar{C}(\tau) = \bar{V}^2 e^{-\tau/\bar{T}} \cos(\Omega\tau) \quad (9)$$

158 where  $\bar{T}$  is the decorrelation timescale and  $\Omega$  accounts for eddies and meanders.

159 The total autocovariance is then given by:

$$C(\tau) = \tilde{C}(\tau) + \bar{C}(\tau) = \left[ \tilde{V}_s^2 + \tilde{V}_{ns}^2 e^{-\tau/\tilde{T}} \right] \times \cos(\omega\tau) + \bar{V}^2 e^{-\tau/\bar{T}} \cos(\Omega\tau) \quad (10)$$

160 This model is then fitted with the autocovariance obtained from our data and averaged  
 161 in bins in the y-direction. The variables  $\tilde{T}$ ,  $\tilde{V}_s$ ,  $\tilde{V}_{ns}$ ,  $\bar{T}$ ,  $\bar{V}$  and  $\Omega$  are estimated to find the best

162 fit. The fit is done using a non linear least square regression (Jones et al. 2001–). Lower  
163 bounds are fixed to zero for all parameters except timescales, for which they are fixed at  
164 one day. The weight is uniform with no dependence on the timelag.

165 Because of drifters displacements across the domain, the time window used for the  
166 computation of Lagrangian autocovariances has to be short enough for the result to be  
167 typical of a specific area, while being long enough to capture the long decorrelation  
168 timescale. For each drifter’s trajectory the velocity time series is split into segments of  
169 length  $T_w$ , overlapping each other by 50%. A time window of 40 day is chosen. Eulerian  
170 mean velocities, averaged in time and zonal direction is interpolated on drifters trajectories  
171 and removed. No significant impacts of this removal were observed on the results for the  
172 fast signal. The autocovariance is computed over each segment and averaged within 50 km  
173 wide meridional bins. Each segment is attributed to a bin depending on the mean position  
174 over the period T. We did not find a significant sensitivity of our results to the length  
175 of the window. The Eulerian autocovariance is computed at each grid point using the  
176 same time windows and bin-averaged meridionally as for the Lagrangian autocovariance.  
177 Autocovariances are then divided by the autocovariance at timelag zero to obtain the  
178 autocorrelation.

### 179 **3. Signatures of internal tides and turbulent jet in Eulerian and Lagrangian perspec-** 180 **tive**

#### 181 *a. Autocorrelation functions*

182 Three main regimes stand out on Lagrangian and Eulerian 2D autocorrelation (function  
183 of timelag and  $y$ ) (Fig.3 first and second column respectively), corresponding to typical  
184 drifters’ trajectories shown in Fig2a, c and e. Autocorrelation at these latitudes of interest  
185 are further shown in Fig. 4. Fast oscillations, corresponding to the internal tides, are seen  
186 in the northern and southern parts of the domain for all autocorrelation functions. In these

187 areas, the signal seems to be dominated by internal tides, with a negligible influence of  
188 the slow advection of the drifters by the balanced flow. No decay of the amplitude of the  
189 oscillations with the time lag can be visually detected south of the domain, especially in  
190 the Eulerian perspective (see Fig. 4, panels e and f) indicating that internal tides are nearly  
191 stationary there. On the contrary, the amplitude of the fast oscillations decays mildly  
192 in the northern area, indicating internal tides non-stationarity. There are no significant  
193 visual differences between Lagrangian and Eulerian autocorrelations in the northern and  
194 southern areas. Conversely, the central area ( $y \in [1000; 2000]$  km) exhibits a fast decay –  
195 especially in the Lagrangian perspective – of fast oscillations combined to a slower general  
196 decay associated with the slower jet turbulence. As observed in drifters trajectories and  
197 velocity time series (Fig. 2, panels c and d), Lagrangian diagnostics diverge from Eulerian  
198 ones in this area. The damping of fast oscillations in the central area occurs over a  
199 much shorter timescale in Lagrangian autocorrelation compared to Eulerian one : fast  
200 oscillations disappear after only a few days ( $\tau \leq 5$  days) in Lagrangian perspective while  
201 they are still visible in the Eulerian one for the largest  $\tau$  (20 days). The decorrelation of the  
202 slower motion is also faster in Lagrangian autocorrelation compared to Eulerian one, and  
203 exhibits a negative lobe around  $\tau \sim 4$  days in the Lagrangian autocorrelation of  $v$ , which  
204 we attribute to the slow evolution of jet meanders. We also note that the autocorrelation  
205 of  $u$  does not decrease toward zero in the jet. Although this aspect is not the focus of our  
206 study, we attribute this to the fact that drifters oversample the meandering jet, resulting in  
207 a larger mean for the zonal velocity compared to the Eulerian mean. The fact that Eulerian  
208 autocorrelation decays more slowly than Lagrangian one is consistent with previous studies  
209 comparing Eulerian and Lagrangian decorrelation timescales (Lumpkin et al. 2002).

210 *b. Estimates of velocity amplitudes and decorrelation timescales*

211 To estimate Eulerian and Lagrangian decorrelation timescales and velocity amplitudes  
212 for both slow and fast motions, we fit the autocovariance from our data (Eulerian and  
213 Lagrangian) to the model given by eq. (10).

214 Eulerian and Lagrangian diagnostics (blue and red lines Fig. 5) show a loss of the  
215 stationarity of internal tides during the crossing of the jet. Eulerian stationary amplitude  
216 (Fig. 5c) exhibits high values relatively to the non-stationary one (Fig. 5d) ( $\sim 0.06 \text{ m s}^{-1}$   
217 versus  $\sim 0.01 \text{ m s}^{-1}$ ) in the south with Eulerian envelope (Fig. 4 e and f) near constant indi-  
218 cating internal tides nearly stationary in this area. During the crossing of the jet, internal  
219 tides loss of stationarity is captured in Eulerian diagnostics as the nonstationary amplitude  
220 becomes larger than the stationary one, increasing up to  $\sim 0.08 \text{ m s}^{-1}$  in the northern part  
221 ( $y$  larger than  $\sim 1700 \text{ km}$ ), while the stationary part decreases slightly ( $\sim 0.05 \text{ m s}^{-1}$ ). A  
222 bump is observed in nonstationary amplitude due to the combined effects of a bump in  
223 stratification in the jet, Coriolis and the loss of stationarity. In this dominantly nonstation-  
224 ary area, nonstationarity timescales are between 10 and 20 days. We note that the Eulerian  
225 envelope in the north (blue lines Fig. 4a and b) does not seem to reach zero but a plateau,  
226 consistent with a remaining stationary component.

227 Lagrangian diagnostics present patterns significantly different from Eulerian ones as  
228 expected from drifters trajectories (Fig. 2 a, c and e) and autocorrelations (Fig. 3). In  
229 the south, the Lagrangian envelope (red lines Fig. 4 e and f) decays faster than Eulerian  
230 one. Lagrangian nonstationary and stationary amplitudes (red lines Fig. 5c and d) present  
231 similar values ( $\sim 0.04 \text{ m s}^{-1}$  for the stationary part and  $\sim 0.03 \text{ m s}^{-1}$  for the nonstationary  
232 part). Nonstationary timescales (Fig. 5a) remain between 10 and 20 days. In the jet area,  
233 the nonstationary amplitude largely dominates as it reaches values around  $\sim 0.08 \text{ m s}^{-1}$   
234 while the stationary part decreases toward values smaller than  $\sim 0.01 \text{ m s}^{-1}$ . Nonstationary  
235 timescale decreases rapidly in this region and reaches 1 day in its center. This apparent non-

236 stationarity in Lagrangian perspective is likely due to a dominant slow motion strongly  
237 advecting the drifters in this area. In the north, we observe a decay of Lagrangian  
238 autocorrelation envelope close to the Eulerian one. Stationary and nonstationary amplitude  
239 are similar to Eulerian ones with non-stationarity dominant. Timescales also have similar  
240 values, between 10 and 20 days. The non-stationarity in this area is captured similarly in  
241 both Lagrangian and Eulerian diagnostics.

242 The slow motion decorrelation timescales (Fig. 5b) reach their lowest values in the  
243 central area,  $\sim 20$  day in Eulerian data and  $\sim 10$  day in Lagrangian outputs. It corresponds  
244 to the area of high amplitude (Fig. 5e). It also coincides with the area of low Lagrangian  
245 non-stationarity timescales which supports an apparent non-stationarity in Lagrangian  
246 diagnostics dominant in this part. As seen in Lagrangian autocorrelation (Fig. 3), oscilla-  
247 tions due to slow motion meanders are observed in the autocorrelation of  $v$  but well fitted  
248 by our model (Veneziani et al. 2004). The fit for the autocorrelation of  $u$  seems however to  
249 fail in the center of the jet with a decorrelation timescale of the slow motion overestimated  
250 in that bin as a tendency towards a value superior to zero is not expected by our model for  
251 slow motion.

252 *c. Sensitivity to the jet's EKE*

253 The sensitivity of internal tide nonstationarity timescales to the jet EKE is investigated  
254 with five numerical simulations of increasing jet's strength as shown by the meridional  
255 distributions of velocity amplitude (Figure 6b).

256 The jet strength, as measured by the velocity amplitude maximum value, varies by  
257 a factor of about 2 across five simulations (Fig.6b). The internal tides' total velocity  
258 amplitude, defined by  $\sqrt{\tilde{V}_s^2 + \tilde{V}_{ns}^2}$ , increases in the northern area with the jet's strength  
259 (Fig.6e). It increases with latitude similarly in both Eulerian and Lagrangian perspectives,  
260 regardless of the region of the domain or the jet's strength.

261 For the 2 most energetic simulations,  $S_3$  and  $S_4$ , both Eulerian and Lagrangian diag-  
262 nostics show a loss of stationarity of internal tides occurs when internal tides cross the  
263 jet. As in the previously studied simulation, the internal tides are nearly stationary in  
264 the southern area in Eulerian amplitudes (continuous lines in Fig. 6c and d) while La-  
265 grangian stationary and nonstationary ones (circular markers in Fig. 6c and d) remain of  
266 similar order. In the jet, Eulerian and Lagrangian nonstationary amplitudes increase while  
267 Lagrangian stationary amplitude drops to zero. Lagrangian timescales (Fig. 6a) reach  
268 minimal values ( $\leq 5$ days) while Eulerian ones remain around or above 10 days in every  
269 simulation. The width of this area increases with the jet's strength. As the drifters move  
270 along with the flow they might capture spatial variations as internal tides' non-stationarity  
271 . This may explain Lagrangian timescales shorter than Eulerian ones in the area where the  
272 slow motion dominates. In the northern area, the same pattern is found for the two cases :  
273 non-stationarity amplitudes and timescales are similar in both framework, the Lagrangian  
274 non-stationarity is not/weakly biased by the drifters' perspective. Interestingly, the inter-  
275 mediate case,  $S_2$  exhibits features similar to  $S_3$  and  $S_4$  in the south and jet but distinct  
276 stationary amplitude and nonstationary timescale. The autocorrelation does not reach a  
277 plateau (stationary amplitude) in the chosen time window. This case is then considered

278 completely nonstationary in the north by our method, with small stationary amplitude and  
 279 overestimated timescale. Contrary to previous cases, the two least energetic simulations,  
 280  $S_0$  and  $S_1$ , show weak loss of stationarity in Eulerian perspective as the stationary am-  
 281 plitude remains dominant for all bins and the nonstationary timescales near the highest  
 282 values allowed in our fitting procedure. Lagrangian stationary amplitude drops to zero in  
 283 the jet as the nonstationary one exhibits a bump in the same area and the timescale drop to  
 284 1 day supporting Lagrangian apparent non-stationarity due to advection even for weakly  
 285 energetic simulations.

#### 286 **4. Lagrangian model for autocovariance and comparison to fitted autocovariance**

##### 287 *a. Theoretical expectation for the fast Lagrangian autocorrelation*

288 We assume that the fast signal is a modulated monochromatic wave propagating in a  
 289 single direction (say  $x$ ) and characterized by a frequency  $\omega$  and wavenumber  $k$ :

$$\tilde{v}(t) = \Re \left\{ \tilde{v}_e(x, t) e^{i(\omega t - kx)} \right\}, \quad (11)$$

290 where  $\tilde{v}_e$  is the slowly varying envelope. Let's consider a parcel traveling with the flow  
 291 with trajectory  $X(t)$ . The autocovariance of  $\tilde{v}$  as measured along the parcel trajectory is  
 292 given by:

$$\tilde{C}_L(\tau) = \langle \tilde{v}(t+\tau) \tilde{v}(t) \rangle, \quad (12)$$

$$= \frac{1}{2} \Re \left\{ \left\langle \tilde{v}_e[X(t+\tau), t+\tau] \tilde{v}_e^*[X(t), t] e^{i[\omega\tau - k(X(t+\tau) - X(t))]} \right\rangle \right\}, \quad (13)$$

293 where we assume that fast oscillation terms ( $\propto e^{\pm 2i\omega t}$ ) are smoothed out by the averaging  
 294 procedure. Neglecting the contribution of the wave velocity to the displacement:  $X(t) =$   
 295  $\int^t \bar{v}(s) ds$ , as well as the spatial dependency of the wave envelope (this point is discussed  
 296 in the discussion, sect. b, below), and further assuming that the envelope of the wave and  
 297 the slow flow are not correlated, we obtain:

$$\tilde{C}_L(\tau) = \Re \left\{ \tilde{C}_E(\tau) \times \left\langle e^{i[\omega\tau - k(X(t+\tau) - X(t))]} \right\rangle \right\}, \quad (14)$$

where  $\tilde{C}_E(\tau)$  is the autocovariance of the envelope. For the latter, we will re-use the model previously introduced in eq. (8), now denoting the Eulerian decorrelation term as  $\tilde{T}_E$ :

$$\tilde{C}_E(\tau) = \tilde{C}(\tau)/\cos(\omega\tau) = \tilde{V}_s^2 + \tilde{V}_{ns}^2 \exp(-\tau/\tilde{T}_E).$$

298 We assume now that the slow flow is a stationary Gaussian process, with a rms amplitude  
 299  $\bar{V}$  (over one direction) and an exponential decorrelation in time with a typical time scale  
 300  $\bar{T}$  – somewhat consistent with the model proposed in section 1, eq. (9) dropping the  
 301  $\cos(\Omega\tau)$  term for simplicity. Such model – sometimes referred as an unbiased correlated  
 302 velocity model in the literature (Gurarie et al.) – corresponds to the time-homogeneous  
 303 Ornstein-Uhlenbeck process.

304 The displacement  $\delta X = X(t + \tau) - X(t)$  is also a Gaussian process with null mean and  
 305 variance given by (Pope 2015, Chap. 12):

$$\langle \delta X(t)^2 \rangle \equiv \sigma_X^2 = 2\bar{T}^2\bar{V}^2 \left[ \tau/\bar{T} - \left( 1 - e^{-\tau/\bar{T}} \right) \right]. \quad (15)$$

306 It is worth noting that the variance of the displacement admits two asymptotic regimes:  
 307  $\sigma_X^2 \rightarrow \bar{V}^2\tau^2$  for  $\tau \ll \bar{T}$ , and  $\sigma_X^2 \rightarrow 2\bar{V}^2\bar{T}\tau$  for  $\tau \gg \bar{T}$ . From this variance for the displace-  
 308 ment, one obtains the final expression for the autocovariance of the fast motion in the  
 309 Lagrangian frame:

$$\tilde{C}_L(\tau) = \tilde{C}_E \int_{-\infty}^{\infty} \cos(\omega\tau - k\delta X) p(\delta X) d\delta X \quad (16)$$

$$= \left( \tilde{V}_s^2 + \tilde{V}_{ns}^2 \exp(-\tau/\tilde{T}_E) \right) \cos(\omega\tau) \int_{-\infty}^{\infty} \cos(k\delta X) \frac{e^{-\delta X^2/(2\sigma_X'^2)}}{\sigma_X' \sqrt{2\pi}} d\delta X \quad (17)$$

$$= \tilde{C} e^{-\sigma_X'^2 k^2/2} = \tilde{C} \exp \left( -k^2 \bar{V}^2 \bar{T}^2 \left[ \tau/\bar{T} - \left( 1 - e^{-\tau/\bar{T}} \right) \right] \right) \quad (18)$$

310 The resulting Lagrangian autocorrelation has no stationary part and decays faster than the  
 311 Eulerian autocorrelation, as follows from the exponentially decay due to drifter transports.  
 312 A non-dimensional parameter  $k\bar{V}\bar{T}$  readily appears in this exponential, which compares  
 313 the time taken by the a drifter to travel a wave length compare to the typical decorrelation

314 time of the slow flow. Several regimes are identified, depending on the effect of the  
 315 advection,  $k^2\sigma^2$ , at a fixed time, typical of the decorrelation of the envelope :

- 316 • Weak advection,  $k^2\sigma^2 \ll 1$  : The signature of the wave signal in the Lagrangian frame  
 317 of reference matches the Eulerian one:  $\tilde{C}_L(\tau) \sim \tilde{C}_E(\tau)$ . Lagrangian stationary and  
 318 non-stationary contributions directly reflect Eulerian ones. If  $\tilde{V}_{ns} \gg \tilde{V}_s$ , Eulerian is  
 319 nonstationary. Amplitudes and non-stationarity timescales are expected to be similar  
 320 in both perspectives. If  $\tilde{V}_{ns} \ll \tilde{V}_s$ , Eulerian signal is stationary.
- 321 • Strong advection,  $k^2\sigma^2 \gg 1$  : the Lagrangian perspective will deform the Eulerian  
 322 one.  $k\bar{V}\bar{T}$  will control the form of the Lagrangian envelope. If  $k\bar{V}\bar{T} \gg 1$  the  
 323 exponential decay of the Lagrangian autocorrelation scales is quadratic in  $\tau$  with  
 324 decay time scale  $1/k\bar{V}$ :  $\tilde{C}_L(\tau) \sim \tilde{V}_s^2 \cos(\omega\tau) \times e^{-k^2\bar{V}^2\tau^2}$ . If  $k\bar{V}\bar{T} \ll 1$  the slow flow  
 325 decorrelation induces a linear exponential decay with decay time scale  $1/k^2\bar{V}^2\bar{T}$ :  
 326  $\tilde{V}_s^2 \cos(\omega\tau) \times e^{-k^2\bar{V}^2\bar{T}\tau}$

327 This predicted form of the autocorrelation in the Lagrangian framework is in qualitative  
 328 agreement with the Lagrangian autocorrelations shown on Fig. 5 and 6. In particular,  
 329 the stationary part of the fitted Lagrangian autocorrelation becomes negligible in a large  
 330 region around the jet latitude. The fact that it is not zero at the very south and very  
 331 north of the domain is due to the fact that the parameter  $k\bar{V}\bar{T}$  is very small in this region,  
 332 associated with a very slow decay of the Lagrangian envelop (see also Fig. 3), which  
 333 implies a non-vanishing stationary fraction as recovered by the model fit from eq. (8).

### 334 *b. Comparison of fitted autocovariances to predicted Lagrangian ones*

335 The predicted Lagrangian autocovariance's envelope (Fig. 7 right column) is computed  
 336 from the fitted Eulerian autocovariance envelope (Fig. 7 left column) following Eq. (18)  
 337 so that it may be compared to the fitted Lagrangian one (Fig. 7 middle column). For  
 338 all simulations ( $S_0$ ,  $S_2$  and  $S_4$  shown in Fig. 7, first, second and third line respectively),

339 the Eulerian autocorrelation envelope's decay rate increases from south to north and with  
 340 the jet's strength as commented previously. This is expected of a loss of stationarity  
 341 as the wave propagates northward. For the fitted Lagrangian autocorrelation however,  
 342 low values of the envelope are reached for small time lags in the jet due to the advection  
 343 in the area. In the northern part the Lagrangian envelope exhibits slower decay rates  
 344 that tend to Eulerian ones. The predicted Lagrangian autocorrelation envelope reaches  
 345 values inferior to 0.1 for time lags smaller than 5 days in the center of the domain which  
 346 is consistent with what is observed in the fitted Lagrangian autocorrelation in a strong  
 347 advection area. In northern and southern area, the advection impact represented in the  
 348 predicted autocorrelation also fits what is observed in fitted Lagrangian autocorrelation  
 349 with decay rates qualitatively close to the Eulerian ones. This decay seems however  
 350 slightly overestimated (values smaller than 0.2 for  $\tau > 30$  days when similar values are  
 351 not reached in Eulerian or Lagrangian fits). Overall, following Eq. (18), the differences  
 352 between Lagrangian and Eulerian can be qualitatively explained as the effect of drifters  
 353 being advected by the slow motion.

354 Depending on the significance of Eulerian non-stationarity and the relative importance  
 355 of  $\tilde{T}_L/\tilde{T}_E$  and  $k^2\sigma^2(\tilde{T}_L)$  (Fig. 8b and c, respectively), the Lagrangian non-stationarity  
 356 timescale is likely due to Eulerian non-stationarity or drifters strong advection by slow  
 357 motion. For simplification sake, both terms will be referred to as  $r_E(\tilde{T}_L)$  and  $r_{adv}(\tilde{T}_L)$   
 358 respectively.

359 In the southern area, the ratio of Eulerian nonstationary and stationary amplitudes  
 360 (Fig. 8a) is smaller than one for all simulations, internal tides area stationary. The advection  
 361 is weak,  $r_{adv}(\tilde{T}_L) \ll 1$ . The Eulerian nonstationary timescale has no significant impact on  
 362 the form of envelope in this area and its estimation is expected not to be significant.  $r_E$   
 363 is found larger than one in this area, however a Lagrangian timescale larger than Eulerian  
 364 one cannot be explained by our model. As stipulated previously, this can be due to

365 an underestimation of the Eulerian timescale. It also could be caused by an estimation  
366 error of Lagrangian nonstationary timescale and/or the result of an inappropriate form  
367 of decay employed for the fit (e.g. linear exponential decay vs quadratic) for Lagrangian  
368 autocovariance as the slow motion decorrelation timescale is of the order of the time  
369 window size (40 days).

370 Northern and central areas illustrate the two different regimes for internal tides non-  
371 stationarity in Lagrangian data, described in the previous subsection. In the north, ratio  
372 of nonstationary and stationary amplitudes is larger than one for  $S_2$ ,  $S_3$  and  $S_4$ , where  
373 nonstationary amplitudes dominates. For least energetic slow motion ( $S_0$  and  $S_1$ ) stationary  
374 tide still dominates but with significant nonstationary contribution. The advection term,  
375  $r_{adv}$  is small in the north and  $r_E$  values are around 1 : the Lagrangian autocovariance is  
376 close to the Eulerian one, following eq.(18). The non-stationarity captured in Lagrangian  
377 perspective corresponds to the one in Eulerian perspective. In the jet, the ratio of Eulerian  
378 nonstationary and stationary amplitudes increases with nonstationary component not yet  
379 dominant. In the same area,  $r_E$  is small as the Lagrangian timescale is small in front of  
380 the Eulerian one, the decorrelation is faster in Lagrangian perspective than in Eulerian  
381 one. This coincides with  $r_{adv}$  around 1, the internal tides' non-stationarity captured in the  
382 Lagrangian perspective is due to advection by slow motion. We call this non-stationarity,  
383 apparent non-stationarity.

## 384 **5. Discussion**

### 385 *a. Lagrangian apparent non-stationarity*

386 We now discuss the reported alteration of the internal tide surface signature in the  
387 Lagrangian perspective in the more general context of observation of ocean high-frequency  
388 dynamics. Low mode internal tides have by definition large vertical scales – similar to  
389 that of the background flow. Advection by the slow flow is of particular importance for

390 discussing the Eulerian/Lagrangian distortion, even though it does not fully capture the  
391 interaction between the slow flow and the internal tide (Dunphy et al. 2017; Savage et al.  
392 2020). A vertical mode expansion of equations of motions linearized around the slow  
393 background flow shows that advection of the internal tide mode is driven by a non-trivial  
394 weighted average of the background flow.

395 This effective advection is expressed as  $H^{-1} \int_{-H}^0 \phi_n^2 \mathbf{U} dz$  (Kelly and Lermusiaux 2016),  
396 where  $\phi_n$  is the standard pressure mode for an internal wave with vertical mode number  $n$   
397 (see also Duda et al., for a more technical approach).

398 Thus, for a surface intensified background flow, the flow advecting the drifter (at the  
399 surface) and the one advecting the internal tide mode is different, explaining why the  
400 Lagrangian observer renders a distorted view of the internal wave signal.

401 For the simulation with moderate jet intensity S2, for instance, the mode 1 effective  
402 advection velocity (computed, but not shown) is of order  $0.2 \text{ m s}^{-1}$  at its maximum, while  
403 the surface velocity is typically greater than  $1 \text{ m s}^{-1}$ : the Eulerian distortion, driven by the  
404 effective advection velocity, is therefore smaller than the Lagrangian distortion, driven by  
405 the difference between this effective advection and the surface velocity transporting the  
406 drifter.

407 This somewhat justifies a central approximation of the theoretical model derived in  
408 section a, where we neglected the advection of the wave by the slow flow.

409 For small scale internal waves on the other hand, ray theory can be used to describe  
410 their propagation through the background flow (Broutman et al. 2004). This approach  
411 shows that wave packets are advected by the local flow, which is associated with a Doppler  
412 shifting of the Eulerian frequency:  $\omega = \hat{\omega} + \mathbf{k} \cdot \mathbf{U}$ , where  $\omega$  and  $\hat{\omega}$  are respectively the wave  
413 absolute (or Eulerian) and intrinsic (as measured in a frame of reference moving with the  
414 slow flow) frequencies,  $\mathbf{k}$  is the wave vector, and  $\mathbf{U}$  is the slow flow.

415 Ignoring advection of the drifter by the wave current, the signal measured by the drifter  
416 coincides with the wave field in the frame comoving with the mean flow with least distortion  
417 in the Lagrangian frame of reference.

418 This situation is opposite to the configuration investigated here, as Lagrangian auto-  
419 correlation exhibits faster decrease with time lag compared to Eulerian auto-correlation,  
420 and the theoretical model proposed here would obviously not be relevant.

421 In a realistic configuration, the range of validity of each of these two regimes (e.g. small  
422 vs large scale waves) remains to be quantified.

423 *b. On internal tide non-stationary spatial envelope*

424 Another assumption of the theoretical model is that the spatial envelope of the wave is  
425 spatially uniform but temporally variable. In reality the envelope of the wave propagates  
426 with the internal tide group speed resulting in spatial variability if a temporal one is  
427 admitted. We assume the typical size of the envelope should however scale as the product  
428 of the group velocity and the Eulerian non-stationary time scale and that this will in  
429 general be larger than several wavelengths. The apparent non-stationarity relies on the  
430 conversion of the spatial variability at the scale of a wavelength and thus do not expect  
431 the spatial variability of the envelope would affect the form (10) at first order. Synthetic  
432 experiments could help verify this point. If necessary, the spatial inhomogeneities of  
433 the wave envelop could be included in the model, at the cost of adding complexity. This,  
434 however, requires additional to characterize these spatial inhomogeneities ( through spatio-  
435 temporal autocovariance), which has not been reported in the context of internal tides – to  
436 our knowledge.

437 *c. Autocorrelations models and stationary/non-stationary decomposition*

438 Several ad-hoc choices have been made regarding the shape of internal tide and slow  
439 motion autocorrelation. Limits to these choices are visible on Figure 4c for slow motions

440 and are speculated to affect estimates of internal tide nonstationary time scales in the  
441 southern part of the domain. The internal tide envelope autocorrelation initially chosen  
442 included a single exponential decaying term instead of the sum of stationary/nonstationary  
443 contributions. We abandoned eventually this choice as it does not naturally lead to the  
444 decomposition of the signal into stationary/non-stationary contributions as well as was  
445 required to consider time scales overly large in stationary cases (>1000 days). One  
446 may also have fitted the more general form (Eq.(18)) to Lagrangian autocorrelations, for  
447 example, and evaluated its relevance compared to the single linear term exponential form.  
448 This would add one more parameter to estimate however and would require to determine  
449 whether this more general form leads to an improvement which we felt was a study on its  
450 own. We did not attempt to do this eventually in favor of a more qualitative assessment  
451 of the theory. Determining what form is more appropriate to describe the Eulerian and  
452 Lagrangian internal envelope autocorrelation is a study on its own that would best reserved  
453 to realistic configurations.

## 454 **6. Conclusion**

455 In order to investigate the use of Lagrangian data to characterize internal tides propagat-  
456 ing through a turbulent jet, we compare Eulerian and Lagrangian internal tides character-  
457 istics in an idealized simulation. Characteristics of mode-1 internal tides were estimated  
458 via fitting data in both perspectives and an internal tide autocovariance envelope including  
459 the sum of a constant stationary contribution and an exponentially decaying nonstationary  
460 one.

461 Near their generation site and far from the jet, internal tides are found to be nearly  
462 stationary in Eulerian perspective. As internal tides propagate through the jet (i.e.  
463 energetic area), the drifters are strongly advected by slow motions which causes  
464 Lagrangian non-stationary timescales to be lower than Eulerian ones. We call this

465 phenomenon, found in Lagrangian perspective, apparent non-stationarity. After crossing  
466 the jet, internal tides propagate in an area of weaker energy but have lost stationarity.  
467 Internal tides non-stationary amplitude is significant there and even dominates in the most  
468 energetic cases. In this area, the intrinsic non-stationarity captured in Eulerian diagnostics  
469 is present similarly in Lagrangian amplitudes and timescales. Regardless of slow motion  
470 amplitude or Eulerian stationarity of internal tides the total amplitude (stationary and  
471 nonstationary components) is successfully recovered in Lagrangian perspective. The  
472 deformation of internal tides characteristics in Lagrangian perspective was qualitatively  
473 predicted by a theoretical model for Lagrangian autocovariances (eq.(18)). This model  
474 modifies Eulerian autocovariances to take into account the advection of drifters.

475  
476 One of the main result of this study is the estimation of the total amplitude in Eulerian  
477 and Lagrangian perspectives using autocovariances and parametric fit instead of non-  
478 parametric spectral analysis. This method has the advantage to avoid the dependence  
479 on an arbitrary choice of frequency band. Indeed, in spectral analysis the chosen band  
480 has a strong impact on evaluating the energy contribution of motions identified by their  
481 frequency (Yu et al. 2019). This choice is further complicated by the variation of the width  
482 of tidal peaks depending on the internal tides' stationarity and drifters advection by slow  
483 motion, in the case of Lagrangian spectra. Parametric spectral analysis could be explored  
484 as an alternative to free from this constraint. The efficiency of our method should also be  
485 investigated in a more realistic set-up.

486 Lagrangian diagnostics and their comparison to Eulerian ones should help to assess  
487 how drifters data could be used, notably in the context of SWOT. As Lagrangian and  
488 Eulerian total amplitudes were found to be similar, Lagrangian estimates could help to  
489 identify where the internal tides contribution to ocean surface energy would be significant.  
490 This leading to where balanced flow and internal tides could be entangled in SWOT

491 data. It involves however a transition from internal tides kinetic energy amplitude to  
492 pressure, which should be investigated. In areas of weak advection, we might be able  
493 to separate stationary and non-stationary amplitudes in Lagrangian data. The theoretical  
494 model developed in this study should help to define regimes for which this separation is  
495 possible. Areas of high non-stationary internal tides contribution and therefore of difficult  
496 prediction of internal tides may thus be flagged. Note that these specific regions are also  
497 the ones where we found a correct estimation of non-stationarity timescales. Again these  
498 preliminary results should be investigated in a realistic set-up, numerical model or in situ  
499 data.

500 This potential information brought by Lagrangian data could also be complementary  
501 material to map internal tides. Mappings of internal tides have been studied from altimetry  
502 (Zaron 2017, 2019). Drifters data, via an estimation of total amplitude, might contribute  
503 to this mapping, setting at least an upper limit to stationary and nonstationary amplitudes.  
504 A direct decomposition of total amplitude in stationary and nonstationary components  
505 may also be derived, in some cases, from drifters data, as noted previously.

506 As anticipated in other studies (Zaron and Elipot 2020), apparent non-stationarity was  
507 found in our Lagrangian data and predicted by our theoretical model, in areas of strong  
508 advection. Areas and regimes for which Lagrangian perspective would deform internal  
509 tides characteristics may be flagged. It could have consequences on the use of Lagrangian  
510 filtering to filter out tidal signal from surface data. Indeed, low decorrelation timescales  
511 translate in the frequency domain by a broadening of tidal peaks which is expected to  
512 complicate the separation of motions by their frequency.

513 The estimation of internal tides contribution in ocean surface energy through the total –  
514 and, in some cases, of stationary and nonstationary – amplitudes from drifters data might  
515 also help to validate realistic models resolving high frequency variability.

516 In the shorter term, a natural extension of our study is to apply our findings to the  
517 analysis of actual drifter trajectories or numerically predicted ones in realistic simulations.  
518 Eulerian outputs from a realistic simulation (LLC4320) have already been compared to  
519 drifters data (Yu et al. 2019). A future study will aim at applying our findings to simulated  
520 drifter trajectories from the same numerical simulation. Similar methods applied to  
521 energetic regions of the globe would allow us to test our method and analytical models to  
522 more realistic set-ups in particular to compare Lagrangian and Eulerian amplitudes and  
523 non-stationarity timescales.

## 524 **References**

525 Broutman, D., J. W. Rottman, and S. D. Eckermann, 2004: Ray Methods for Internal  
526 Waves in the Atmosphere and Ocean. **36 (1)**, 233–253, doi:10.1146/annurev.fluid.36.  
527 050802.122022.

528 Buijsman, M. C., B. K. Arbic, J. G. Richman, J. F. Shriver, A. J. Wallcraft, and L. Zamudio,  
529 2017: Semidiurnal internal tide incoherence in the equatorial p acific. *Journal of*  
530 *Geophysical Research: Oceans*, **122 (7)**, 5286–5305.

531 Davis, R., 1983: Oceanic property transport, lagrangian particle statistics, and their  
532 prediction. *Journal of Marine Research*, **41 (1)**, 163–194.

533 Davis, R. E., 1985: Drifter observations of coastal surface currents during CODE: The  
534 method and descriptive view. *J. Geophys. Res.*, **90(C3)**, 4741–4755.

535 Duda, T. F., Y.-T. Lin, M. Buijsman, and A. E. Newhall, ????: Internal Tidal Modal Ray  
536 Refraction and Energy Ducting in Baroclinic Gulf Stream Currents. **48 (9)**, 1969–1993,  
537 doi:10.1175/JPO-D-18-0031.1.

538 Dunphy, M., A. L. Ponte, P. Klein, and S. Le Gentil, 2017: Low-mode internal tide  
539 propagation in a turbulent eddy field. *Journal of Physical Oceanography*, **47** (3), 649–  
540 665.

541 Elipot, S., R. Lumpkin, R. C. Perez, J. M. Lilly, J. J. Early, and A. M. Sykulski, 2016: A  
542 global surface drifter data set at hourly resolution. *Journal of Geophysical Research:*  
543 *Oceans*, **121** (5), 2937–2966.

544 Elipot, S., R. Lumpkin, and G. Prieto, 2010: Modification of inertial oscillations by the  
545 mesoscale eddy field. *Journal of Geophysical Research: Oceans*, **115** (C9).

546 Fu, L.-L., D. Alsdorf, R. Morrow, E. Rodriguez, and N. Mognard, 2012: Swot: The surface  
547 water and ocean topography mission: Wide-swath altimetric elevation on earth. Tech.  
548 rep., Pasadena, CA: Jet Propulsion Laboratory, National Aeronautics and Space . . . .

549 Garrett, C., and E. Kunze, 2007: Internal tide generation in the deep ocean. *Annu. Rev.*  
550 *Fluid Mech.*, **39**, 57–87.

551 Gurarie, E., C. H. Fleming, W. F. Fagan, K. L. Laidre, J. Hernández-Pliego, and  
552 O. Ovaskainen, ????: Correlated velocity models as a fundamental unit of animal  
553 movement: Synthesis and applications. **5** (1), 13, doi:10.1186/s40462-017-0103-3.

554 Jones, E., T. Oliphant, P. Peterson, and Coauthors, 2001–: SciPy: Open source scientific  
555 tools for Python: Least square regression. [Available online at [https://docs.scipy.org/  
556 doc/scipy/reference/generated/scipy.optimize.curve\\_fit.html](https://docs.scipy.org/doc/scipy/reference/generated/scipy.optimize.curve_fit.html)].

557 Kelly, S. M., and P. F. J. Lermusiaux, 2016: Internal-tide interactions with the Gulf  
558 Stream and Middle Atlantic Bight shelfbreak front. **121** (8), 6271–6294, doi:10.1002/  
559 2016JC011639.

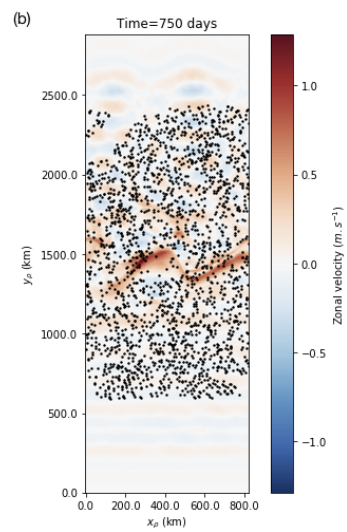
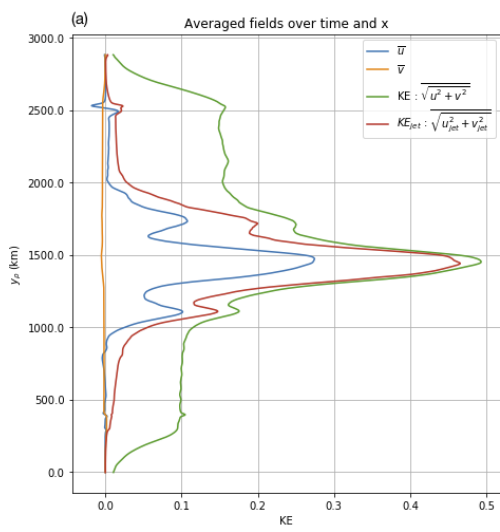
560 LaCasce, J., 2008: Statistics from lagrangian observations. *Progress in Oceanography*,  
561 **77** (1), 1–29.

- 562 Lumpkin, R., A.-M. Treguier, and K. Speer, 2002: Lagrangian eddy scales in the northern  
563 atlantic ocean. *Journal of physical oceanography*, **32 (9)**, 2425–2440.
- 564 Middleton, J. F., 1985: Drifter spectra and diffusivities. *Journal of Marine Research*,  
565 **43 (1)**, 37–55.
- 566 Morrow, R., and Coauthors, 2019: Global observations of fine-scale ocean surface topog-  
567 raphy with the surface water and ocean topography (swot) mission. *Frontiers in Marine*  
568 *Science*, **6**, 232.
- 569 Nash, J. D., S. M. Kelly, E. L. Shroyer, J. N. Moum, and T. F. Duda, 2012a: The unpre-  
570 dictable nature of internal tides on continental shelves. *Journal of Physical Oceanog-*  
571 *raphy*, **42 (11)**, 1981–2000.
- 572 Nash, J. D., E. L. Shroyer, S. M. Kelly, M. E. Inall, T. F. Duda, M. D. Levine, N. L. Jones,  
573 and R. C. Musgrave, 2012b: Are any coastal internal tides predictable? *Oceanography*,  
574 **25 (2)**, 80–95.
- 575 Nelson, A. D., B. K. Arbic, E. D. Zaron, A. C. Savage, J. G. Richman, M. C. Buijsman, and  
576 J. F. Shriver, 2019: Toward realistic nonstationarity of semidiurnal baroclinic tides in a  
577 hydrodynamic model. *Journal of Geophysical Research: Oceans*, **124 (9)**, 6632–6642.
- 578 Ponte, A. L., and P. Klein, 2015: Incoherent signature of internal tides on sea level in  
579 idealized numerical simulations. *Geophysical Research Letters*, **42 (5)**, 1520–1526.
- 580 Ponte, A. L., P. Klein, M. Dunphy, and S. Le Gentil, 2017: Low-mode internal tides and  
581 balanced dynamics disentanglement in altimetric observations: Synergy with surface  
582 density observations. *Journal of Geophysical Research: Oceans*, **122 (3)**, 2143–2155.
- 583 Pope, S. B., 2015: *Turbulent Flows*. Cambridge Univ. Press, 771 pp.
- 584 Ray, R. D., and E. D. Zaron, 2016: M2 internal tides and their observed wavenumber  
585 spectra from satellite altimetry. *Journal of Physical Oceanography*, **46 (1)**, 3–22.

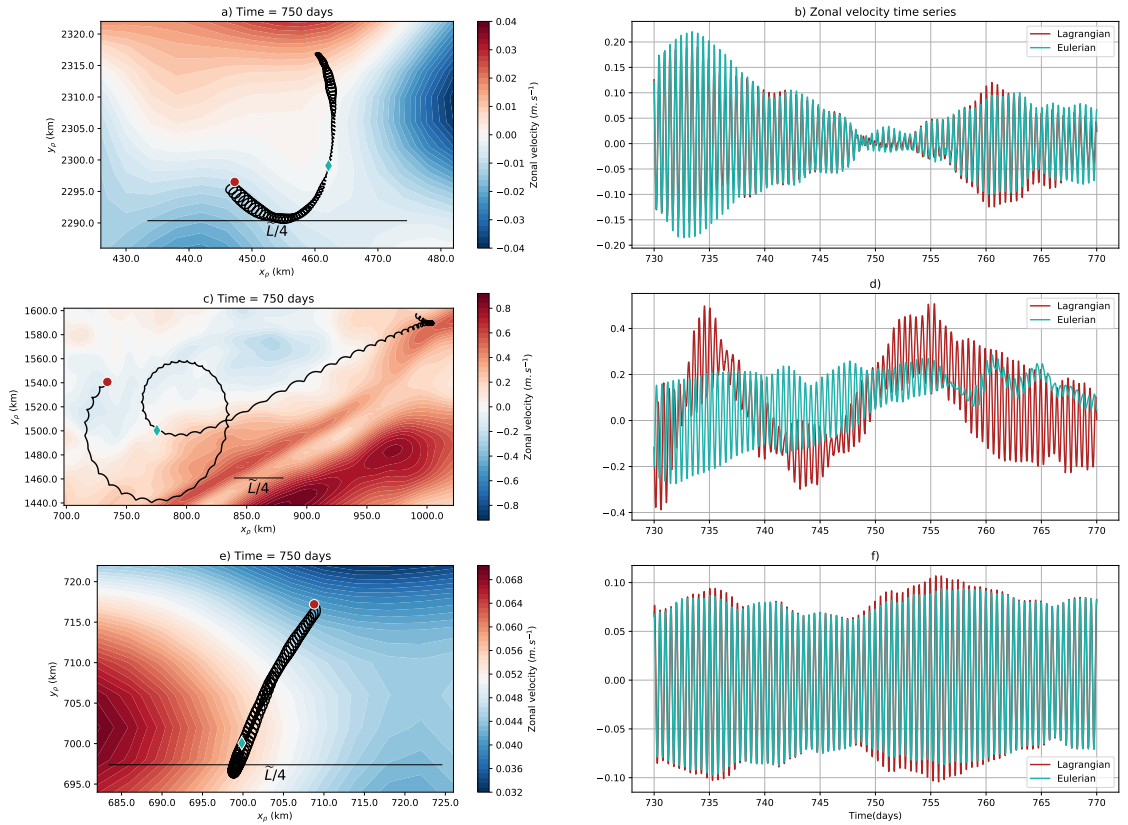
- 586 Savage, A., and Coauthors, 2020: Low-mode internal tides and small scale surface  
587 dynamics in the swot cal/val region. *Ocean Sciences Meeting 2020*, AGU.
- 588 Savva, M. A., and J. Vanneste, 2018: Scattering of internal tides by barotropic quasi-  
589 geostrophic flows. *Journal of Fluid Mechanics*, **856**, 504–530.
- 590 Veneziani, M., A. Griffa, A. M. Reynolds, and A. J. Mariano, 2004: Oceanic turbulence  
591 and stochastic models from subsurface lagrangian data for the northwest atlantic ocean.  
592 *Journal of physical oceanography*, **34 (8)**, 1884–1906.
- 593 Whalen, C. B., C. de Lavergne, A. C. N. Garabato, J. M. Klymak, J. A. Mackinnon, and  
594 K. L. Sheen, 2020: Internal wave-driven mixing: governing processes and consequences  
595 for climate. *Nature Reviews Earth & Environment*, **1 (11)**, 606–621.
- 596 Yu, X., A. L. Ponte, S. Elipot, D. Menemenlis, E. Zaron, and R. Abernathey, 2019: Surface  
597 kinetic energy distributions in the global oceans from a high-resolution numerical model  
598 and surface drifter observations. *Geophys. Res. Lett.*
- 599 Zaron, E. D., 2017: Mapping the nonstationary internal tide with satellite altimetry.  
600 *Journal of Geophysical Research: Oceans*, **122 (1)**, 539–554.
- 601 Zaron, E. D., 2019: Baroclinic tidal sea level from exact-repeat mission altimetry. *Journal*  
602 *of Physical Oceanography*, **49 (1)**, 193–210.
- 603 Zaron, E. D., and S. Elipot, 2020: An assessment of global ocean barotropic tide models  
604 using geodetic mission altimetry and surface drifters. *Journal of Physical Oceanogra-*  
605 *phy*.

## List of Figures

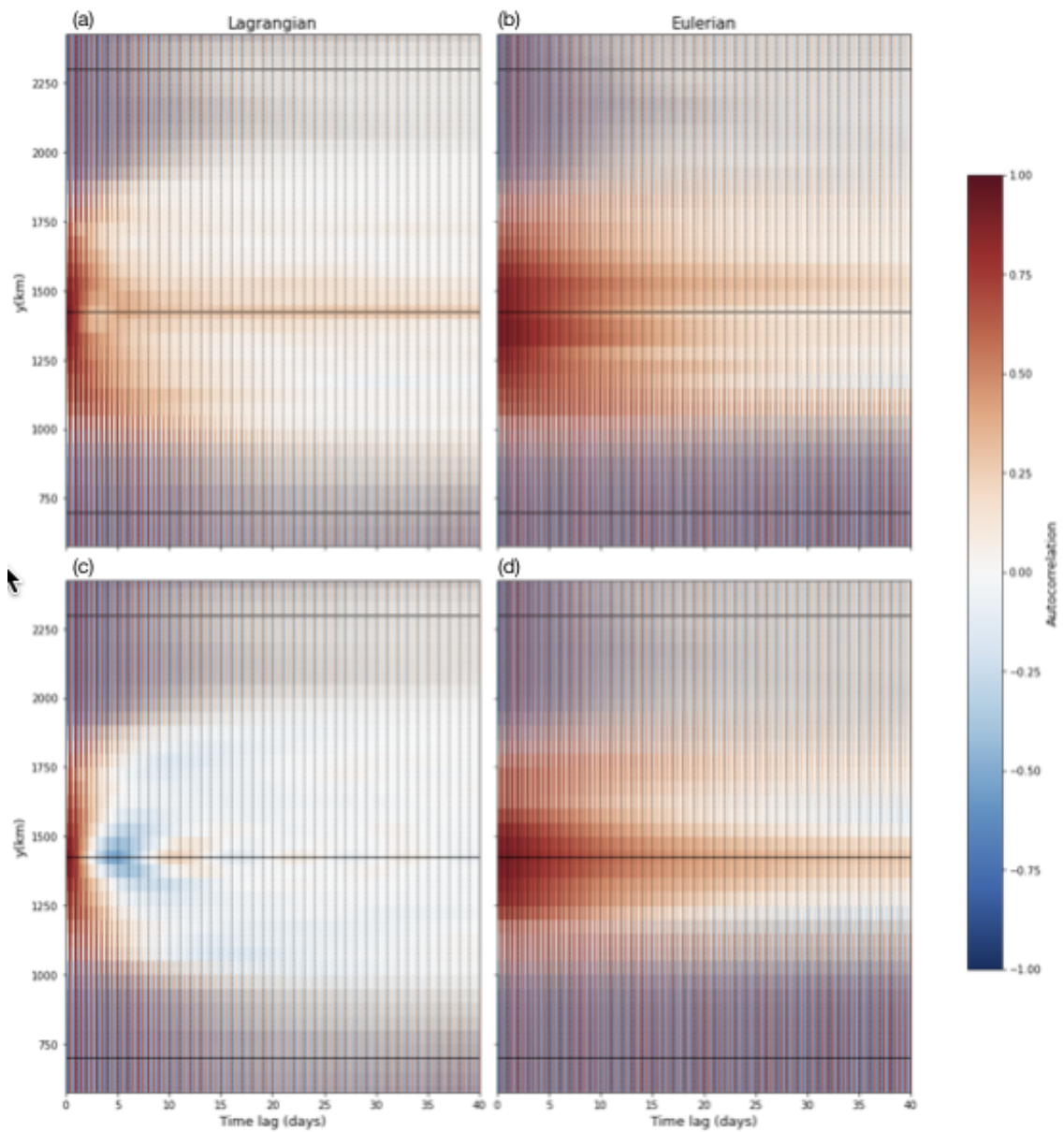
606		
607	<b>Fig. 1.</b>	(a) : Mean field of zonal (blue line), meridional (orange line), total (green) and low-passed (red) velocity amplitudes ; (b) : Zonal velocity at t=750 days (color) with positions of 1/4 of the drifters at the same time represented by black dots. . . . . 29
608		
609		
610	<b>Fig. 2.</b>	Trajectories of 3 drifters in three different area of the domain (north (a and b), central (c and d) and south (e and f)) over a period of 40 days and corresponding time series. Left column : Trajectory of each the drifter (black line) with the zonal velocity in the background. The red circle represents the position of the drifter at t0 and the blue diamond the position at mid period. A black straight line is plotted representing a quarter of the wavelength. Right column : Zonal velocity time series along the drifter trajectory in red and at a fixed position (blue diamond in the left figure) in blue. . . . . 30
611		
612		
613		
614		
615		
616		
617		
618	<b>Fig. 3.</b>	Autocorrelation of u (a and b) and v (c and d) computed from Lagrangian outputs (a and c) and Eulerian one (right column : b and d). The y-axis corresponds to the y bins in which the autocorrelation have been averaged. In the x-axis is the time lag. Horizontal black lines indicate the three latitudes of interest discussed in the paper (see Figs. 2 and 4) . . . . . 31
619		
620		
621		
622		
623	<b>Fig. 4.</b>	Autocorrelation at fixed bin in three different area : north (a and b), center (c and d) and south (e and f) of the domain). The Eulerian and Lagrangian autocorrelation derived from our data are represented respectively in blue and red. The autocorrelation corresponding to the best fit of our theoretical model with the autocovariance are plotted in grey dashed lines. Corresponding values of the fitted parameters are indicated in each panel. . . . . 32
624		
625		
626		
627		
628		
629	<b>Fig. 5.</b>	Estimated eulerian (blue lines) and Lagrangian (red lines with circular markers) non-stationarity, $\tilde{T}$ (a) and decorrelation of the balanced flow, $\bar{T}$ (b) timescales and fast and slow components amplitudes, $\tilde{V}_{ns}$ (c), $\tilde{V}_s$ (d) and $\bar{V}$ (e). The estimates are found by fitting the theoretical model (Eq.(18)) to the autocorrelation of u (dashed lines) and v (continuous lines). . . . . 33
630		
631		
632		
633		
634	<b>Fig. 6.</b>	Estimated parameters for five simulations. (a) Lagrangian and Eulerian internal tides nonstationary timescales, $\tilde{T}$ . (c), (d) and (e) : Fast components nonstationary and stationary velocity amplitudes, $\tilde{V}_{ns}$ and $\tilde{V}_s$ and total amplitude, $\sqrt{\tilde{V}_{ns}^2 + \tilde{V}_s^2}$ . Slow component velocity amplitude, $\bar{V}$ (b) is also represented. Timescales lower than 1 day and larger than 40 days were not allowed by our fitting procedure. . . . . 34
635		
636		
637		
638		
639	<b>Fig. 7.</b>	Amplitude of the envelop of fast oscillation in autocorrelation functions for 3 simulations (corresponding to rows). From top to bottom the jet's strength increases. The envelope of the fitted Eulerian (left column) and Lagrangian (middle column) autocorrelation as well as the predicted Lagrangian autocorrelation (right column) are plotted. . . . . 35
640		
641		
642		
643		
644	<b>Fig. 8.</b>	Ratio $\tilde{V}_{ns}/\tilde{V}_s$ (a) and $\tilde{T}_L/\tilde{T}_E$ (b) as well as the term in the exponential (Eq. (18)), $k^2\sigma(\tilde{T}_L)$ , (c) are represented. . . . . 36
645		



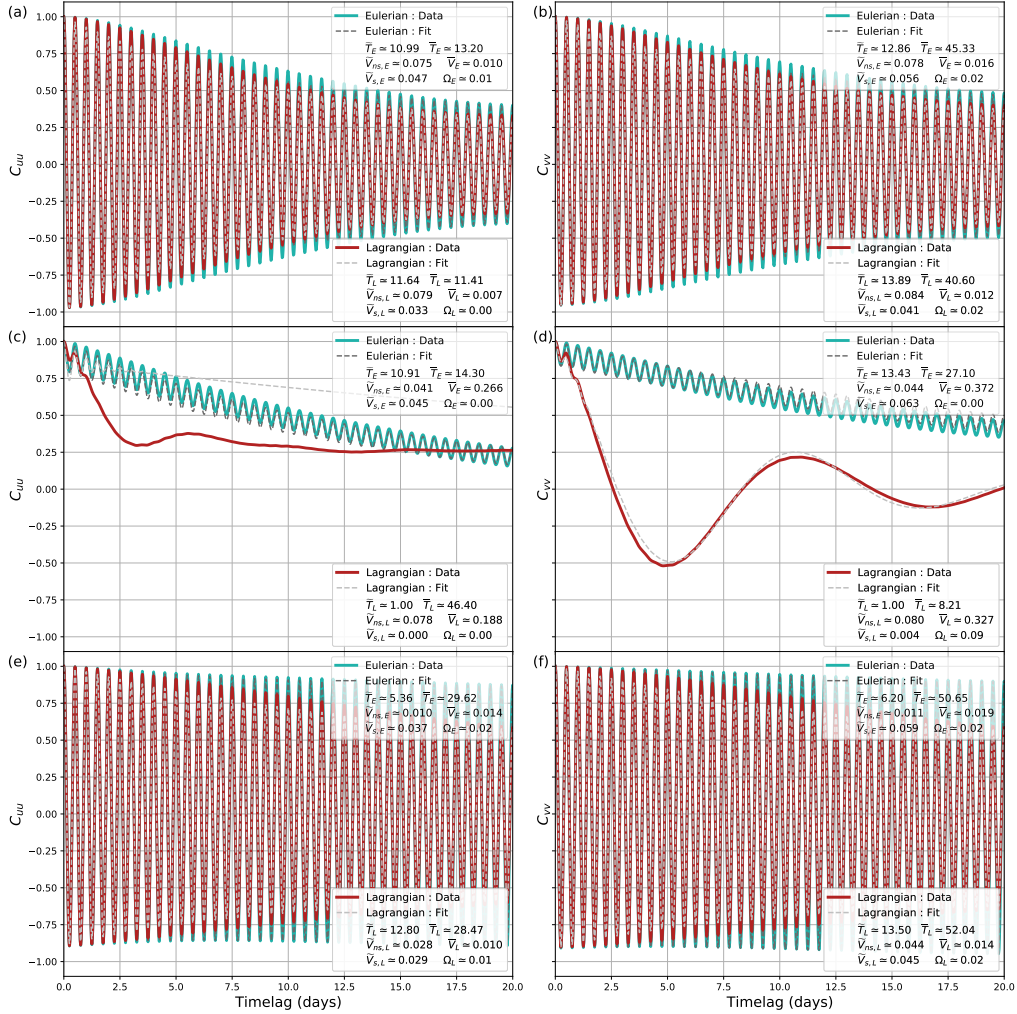
646 Figure 1. (a) : Mean field of zonal (blue line), meridional (orange line), total (green) and low-passed  
 647 (red) velocity amplitudes ; (b) : Zonal velocity at t=750 days (color) with positions of 1/4 of the drifters  
 648 at the same time represented by black dots.



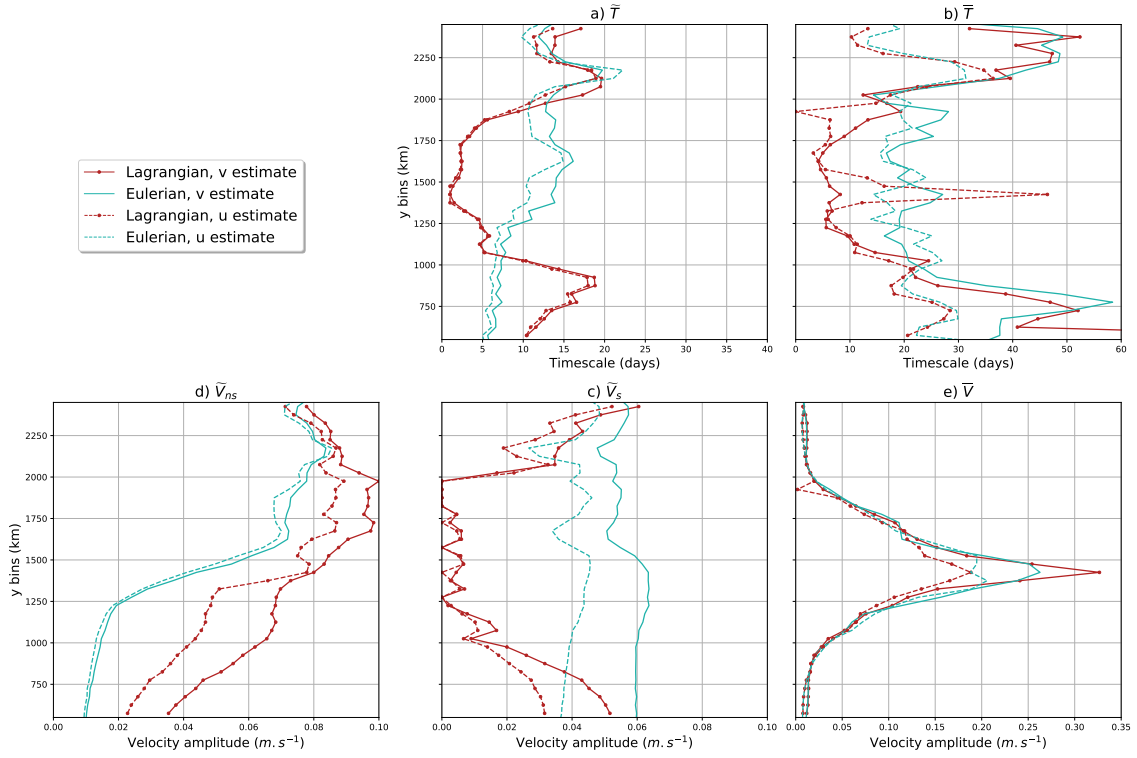
649 Figure 2. Trajectories of 3 drifters in three different area of the domain (north (a and b), central  
 650 (c and d) and south (e and f)) over a period of 40 days and corresponding time series. Left column  
 651 : Trajectory of each the drifter (black line) with the zonal velocity in the background. The red circle  
 652 represents the position of the drifter at  $t_0$  and the blue diamond the position at mid period. A black  
 653 straight line is plotted representing a quarter of the wavelength. Right column : Zonal velocity time  
 654 series along the drifter trajectory in red and at a fixed position (blue diamond in the left figure) in blue.



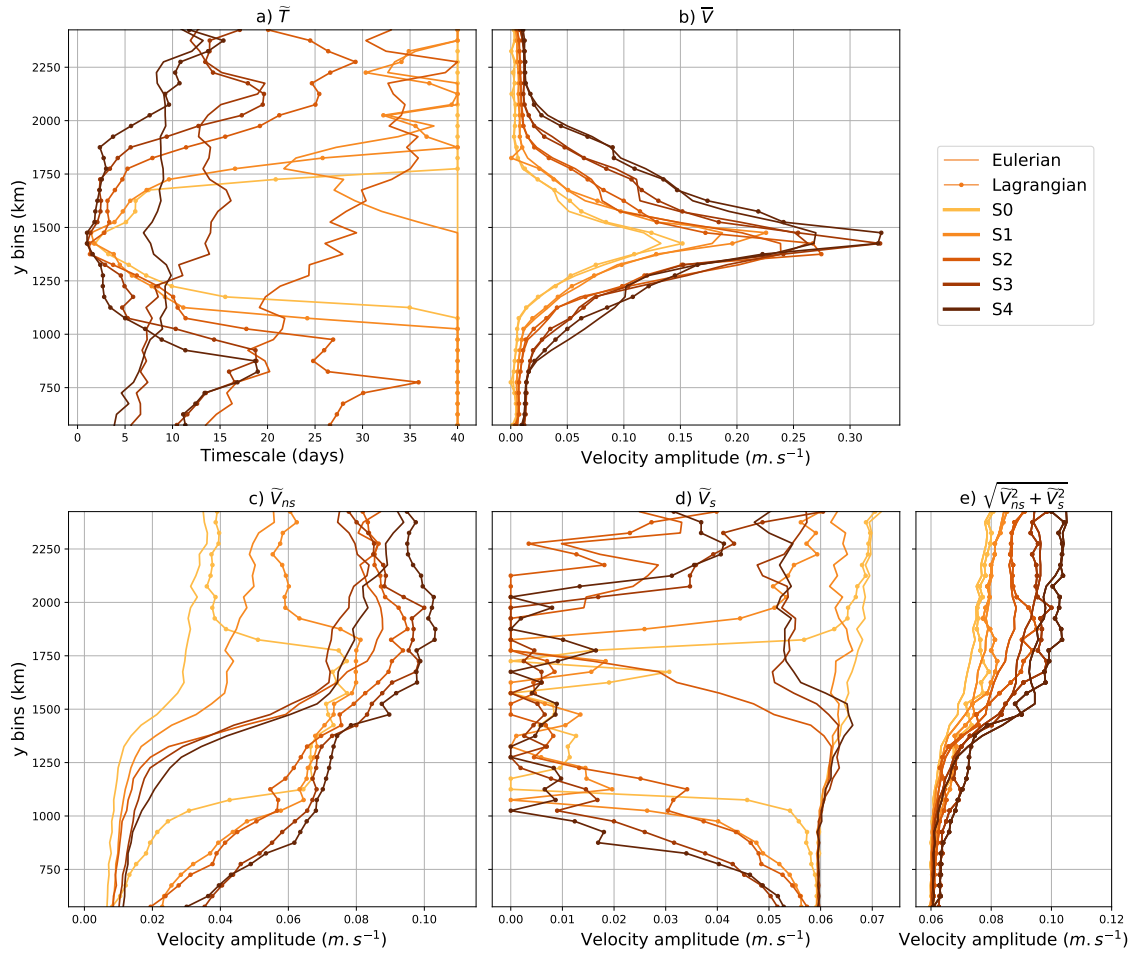
655 Figure 3. Autocorrelation of u (a and b) and v (c and d) computed from Lagrangian outputs (a  
 656 and c) and Eulerian one (right column : b and d). The y-axis corresponds to the y bins in which the  
 657 autocorrelation have been averaged. In the x-axis is the time lag. Horizontal black lines indicate the  
 658 three latitudes of interest discussed in the paper (see Figs. 2 and 4)



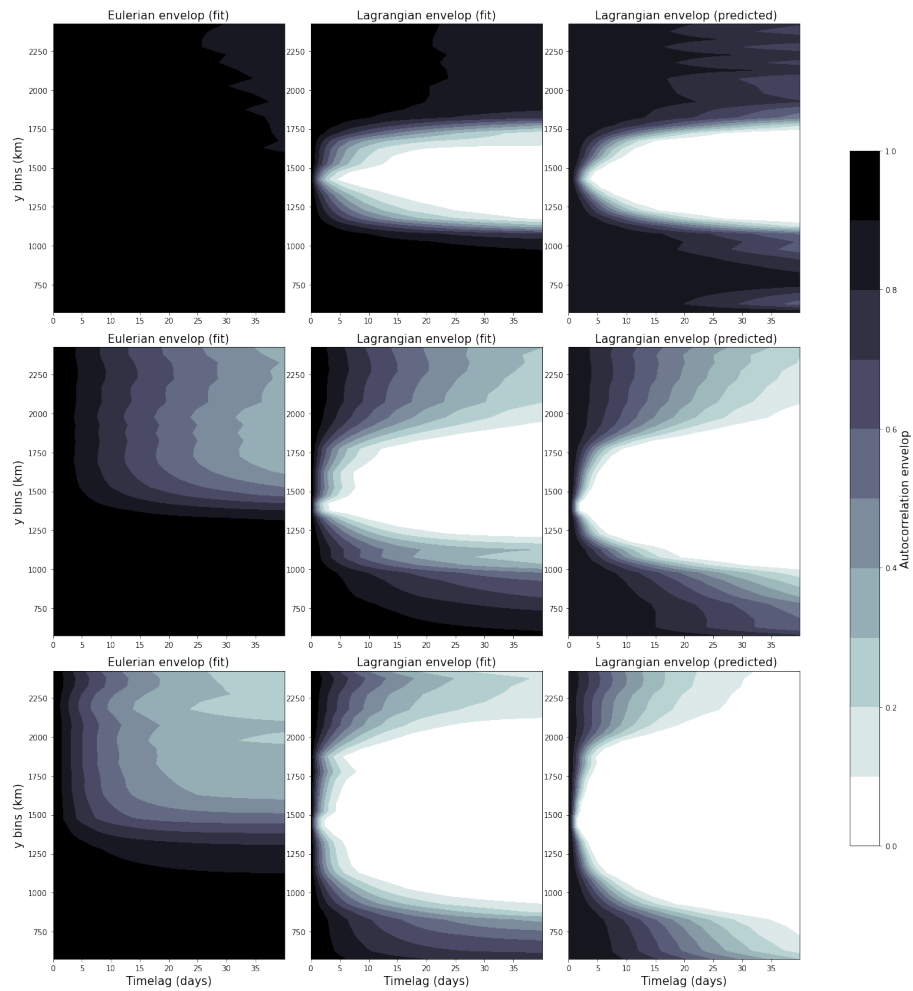
659 Figure 4. Autocorrelation at fixed bin in three different area : north (a and b), center (c and d) and  
660 south (e and f) of the domain). The Eulerian and Lagrangian autocorrelation derived from our data  
661 are represented respectively in blue and red. The autocorrelation corresponding to the best fit of our  
662 theoretical model with the autocovariance are plotted in grey dashed lines. Corresponding values of  
663 the fitted parameters are indicated in each panel.



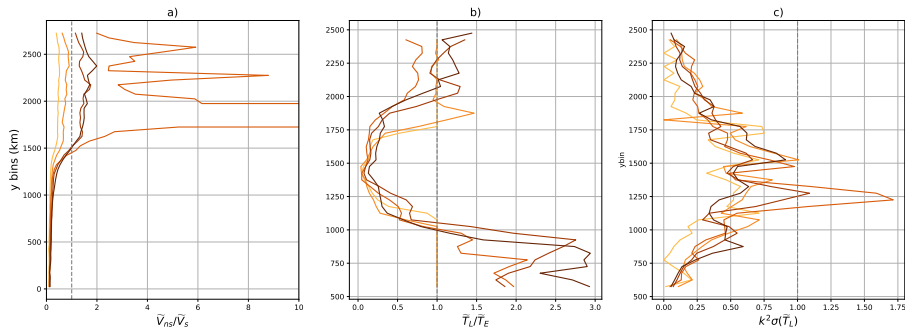
664 Figure 5. Estimated eulerian (blue lines) and Lagrangian (red lines with circular markers) non-  
 665 stationarity,  $\bar{T}$  (a) and decorrelation of the balanced flow,  $\bar{T}$  (b) timescales and fast and slow components  
 666 amplitudes,  $\tilde{V}_{ns}$  (c),  $\tilde{V}_s$  (d) and  $\bar{V}$  (e). The estimates are found by fitting the theoretical model (Eq.(18))  
 667 to the autocorrelation of u (dashed lines) and v (continuous lines).



668 Figure 6. Estimated parameters for five simulations. (a) Lagrangian and Eulerian internal tides  
 669 nonstationary timescales,  $\tilde{T}$ . (c), (d) and (e) : Fast components nonstationary and stationary velocity  
 670 amplitudes,  $\tilde{V}_{ns}$  and  $\tilde{V}_s$  and total amplitude,  $\sqrt{\tilde{V}_{ns}^2 + \tilde{V}_s^2}$ . Slow component velocity amplitude,  $\bar{V}$  (b)  
 671 also represented. Timescales lower than 1 day and larger than 40 days were not allowed by our fitting  
 672 procedure.



673 Figure 7. Amplitude of the envelop of fast oscillation in autocorrelation functions for 3 simulations  
 674 (corresponding to rows). From top to bottom the jet's strength increases. The envelope of the  
 675 fitted Eulerian (left column) and Lagrangian (middle column) autocorrelation as well as the predicted  
 676 Lagrangian autocorrelation (right column) are plotted.



677 Figure 8. Ratio  $\tilde{V}_{ns}/\tilde{V}_s$  (a) and  $\tilde{T}_L/\tilde{T}_E$  (b) as well as the term in the exponential (Eq. (18)),  $k^2\sigma(\tilde{T}_L)$ ,  
 678 (c) are represented.